

INFERRING INTERSTELLAR MEDIUM DENSITY, TEMPERATURE, AND METALLICITY FROM TURBULENT H II REGIONS

LARRANCE XING^{1,*}, NICHOLAS CHOUSTIKOV², HARLEY KATZ^{1,3,*}, & ALEX J. CAMERON^{4,5,2}¹Department of Astronomy & Astrophysics, University of Chicago, 5640 S Ellis Avenue, Chicago, IL 60637, USA²Sub-department of Astrophysics, University of Oxford, Keble Road, Oxford OX1 3RH, United Kingdom³Kavli Institute for Cosmological Physics, University of Chicago, Chicago IL 60637, USA⁴Cosmic Dawn Center (DAWN), Copenhagen, Denmark and⁵Niels Bohr Institute, University of Copenhagen, Jagtvej 128, DK-2200, Copenhagen, Denmark*Version February 4, 2026*

ABSTRACT

Reliable nebular emission line diagnostics are essential for accurately inferring the physical properties (e.g. electron temperature, density, pressure, and metallicity) of H II regions from spectra. When interpreting spectra, it is typical to adopt a single zone model, e.g. at fixed density, pressure, or temperature, to infer H II region properties. However, such an assumption may not fully capture the complexities of a turbulent interstellar medium. To understand how a complex density field driven by supersonic turbulence impacts nebular emission lines, we simulate 3D H II regions surrounding a single O star, both with and without supersonic turbulence. We find that turbulence directly impacts the values of common strong line ratios. For example turbulent H II regions exhibit systematically higher [N II]/H α , lower [O III]/H β , and lower O32, compared to homogeneous H II regions with the same mean density and ionizing source. These biases can impact inferences of metallicity, ionization parameter, excitation, and ionization source. For our choice of turbulence, direct T_e method metallicity inferences are biased low, by up to 0.1 dex, which is important for metallicity studies, but not enough to explain the abundance discrepancy problem. Finally, we show that large differences between measured electron densities emerge between infrared, optical, and UV density indicators. Our results motivate the need for large grids of turbulent H II regions models that span the range of conditions seen at both high and low redshift to better interpret observed spectra.

Subject headings: ISM, galaxy formation

1. INTRODUCTION

Nebular emission line diagnostics represent a powerful probe of the physical properties of the interstellar medium (ISM). The electron temperature, density, pressure, and metallicity of H II regions can all be probed by various combinations of emission lines that originate in ionized gas (Kewley et al. 2019; Kewley, Nicholls & Sutherland 2019). Likewise, diagnostics from low-ionization state atoms and molecules can be used to trace similar properties in neutral or diffuse ionized gas.

The physical conditions (e.g. electron temperature, electron number density, and ion number density) of the ISM strongly impact the emission from H II regions. For example, an ion can be used to trace electron temperature in an H II region if the species is both abundant enough and the first two excited states are at low enough energy so that they can be sufficiently populated by collisional excitation. An example of such an ion is O $^{++}$. O $^{++}$ has an ionization energy of 35.1 eV which is low enough to be photoionized by stars, while the next ionization state requires 54.9 eV, which is typically higher than that of photons emitted by a massive, metal-enriched O-star — hence the ion is sufficiently abundant. Next, the first two excited state (from the 3P ground state) are 1D and 1S , which require ~ 2.5 eV and ~ 5.3 eV, respectively to populate. Assuming the electron velocity distribution function is well modeled by a Maxwell-

Boltzmann distribution, which depends only on temperature, the ratio of emission from these two states (i.e. the 5007 Å and 4363 Å lines) probe the electron temperature. Other ions with structure suitable for tracing electron temperature that are commonly observed in H II regions include N $^+$, O $^+$, S $^{++}$, etc. Similarly, electron density can be probed, for example, by ions that have closely-spaced doublet states (e.g. O $^+$, S $^+$, Ar $^{+++}$). Because the doublet state requires approximately the same excitation energy, the difference in emissivity is dictated by differences in the Einstein coefficient for spontaneous de-excitation and collisional de-excitation. The former is measured from quantum mechanical calculations and the latter represents the probe of electron density. The simplicity of this physics makes such calculations readily applicable to observed galaxy spectra with open-source software (e.g. Dere et al. 1997; Luridiana, Morisset & Shaw 2015).

A key assumption about these calculations is that all of the emission originates from a single “zone” that has a uniform density, temperature, metallicity, etc. This assumption is untrue both within individual H II regions (e.g. Rubin 1968) as well as across a galaxy as a whole (e.g. Kobulnicky, Kennicutt & Pizagno 1999; Harikane et al. 2025). To address this issue, there are two approaches. First, numerous codes have been developed that statistically apply multi-zone models to observed spectra to infer galaxy and H II region properties (e.g. Lebouteiller & Ramambason 2022; Marconi et al. 2024). For such inference, either the distribution function of

^{*}E-mail: larrance@uchicago.edu^{*}E-mail: harleykatz@uchicago.edu

H II region properties must be parametrized or for non-parametric models, a cap or regularization must be applied to limit the number of zones. Alternatively, one can attempt to forward model the detailed structure of individual H II regions or a whole galaxy (comprised of multiple H II regions). While modeling entire galaxies remains difficult, public codes such as CLOUDY (Ferland et al. 1998; Chatzikos et al. 2023) or MAPPINGS (Dopita & Sutherland 1996; Sutherland et al. 2018) have made H II region models widely accessible and they have been extremely successful in being able to reproduce the distribution of observed galaxy and H II region properties seen in large surveys (e.g. Kewley et al. 2001).

However, photoionization models of H II regions have some key limitations. First, they often assume simplified geometries (e.g. spherical or plane-parallel) and either constant density or pressure¹. It is now well established that the geometry of an H II region can have significant effects on the resultant emission (e.g. Jin, Kewley & Sutherland 2022b). Second, typical photoionization models assume that the cloud is in equilibrium (although c.f. Gnat & Sternberg 2007; Kumar & Chen 2025 in the context of the circumgalactic medium — CGM). However, this assumption may break down in the case where the timescale for the ionization front to reach the Strömgren radius becomes shorter than the main-sequence lifetime of massive stars or if the cooling time is shorter than the recombination time (see e.g. Richings et al. 2022; Katz et al. 2022 for discussion of the latter). Finally, the ISM is known to be turbulent and when the turbulence is supersonic, emission line ratios can differ from a static medium (e.g. Gray & Scannapieco 2017).

The primary reason more complicated models of H II regions and galaxies have been less explored is that they are computationally much more expensive. While grids of millions of, for example, CLOUDY models can be readily computed on modern supercomputer architectures, the same is not true for 3D H II region models. Nevertheless, there are now numerous codes that can address the key issues with photoionization models (e.g. Gray, Scannapieco & Kasen 2015; Ziegler 2018; Jin, Kewley & Sutherland 2022a; Katz 2022; Smith et al. 2023; Chan et al. 2025; McClymont, Smith & Tacchella 2025), with a subset able to couple the detailed non-equilibrium chemistry to the hydrodynamics.

The purpose of this work is to consider one step beyond a simplistic H II region model and quantify how emission line diagnostics respond to a non-trivial H II region geometry. We focus on line-ratio diagnostics for metallicity and electron density. In our idealized experiments, we first compute the emission from the H II region around a single O star embedded in a uniform density medium. Next, we drive supersonic turbulence around the star, recompute the emission, and compare the resultant line ratios to the homogeneous case. This allows us to estimate the impact of an inhomogeneous density structure on nebular emission line diagnostics.

This paper is arranged as follows. We describe the numerical simulations and the methods for measuring metallicity and density in Section 2. We present our

¹ Note that this is not true of all photoionization models in the literature but this is anecdotally a reasonable description of what is generally assumed.

results in Section 3, and discuss how our results compare with previous studies pertaining to line ratio diagnostics in Section 4.

2. NUMERICAL SIMULATIONS

All simulations in this work are run with the RAMSES-RTZ code (Katz 2022) and the PRISM ISM model (Katz et al. 2022), which is a fork of RAMSES (Teyssier 2002) and RAMSES-RT (Rosdahl et al. 2013; Rosdahl & Teyssier 2015). RAMSES-RTZ has been benchmarked directly against CLOUDY in numerous ways and shown to reproduce the emission line luminosities of constant-density H II regions to better than 10% on average (Katz 2022; Katz et al. 2024), which is consistent with the differences seen between CLOUDY and MAPPINGS (D’Agostino et al. 2019). We consider two types of simulations: constant density (homogeneous) models and turbulent boxes. Our numerical setup shares many similarities with the work of Jin, Kewley & Sutherland (2022b), with a key difference being that we drive turbulence through the box to obtain a complex density distribution rather than adopting a fractal geometry.

2.1. Calibrations with Homogeneous Boxes

Before we can study the impact of a non-trivial density distribution on emission line ratios, it is crucial to calibrate our emission line diagnostics predicted by RAMSES-RTZ for a constant density medium. To this end, we begin by placing a single O4V star, modeled as a blackbody with a temperature of 42,900 K², at the center of a computational domain with side length 10 pc, with a constant density. The source emits 1.25×10^{50} ionizing photons per second. Our homogeneous models range from $10\text{--}10,000 \text{ H cm}^{-3}$ in density. The domain is split into 256^3 elements and the box size is varied depending on density so that the H II region is ionization-bounded. The simulation is then evolved until the ionization front reaches the Strömgren radius and the system reaches steady-state. Note that here we do not model the hydrodynamics of the system and only consider the impact of photoionization and photoheating. In other words, the gas distribution remains static (ignoring radiation pressure and the over-pressurization of the H II region from photoheating). Hence, our setup is as similar as possible to standard photoionization models with the only difference being the 3D geometry. The radiation is modeled in eight frequency bins following Kimm et al. (2017); Katz et al. (2024). We consider five different metallicities, 0.01, 0.05, 0.1, 0.5, and $1 Z_\odot$ with metal abundance patterns adopted from Asplund et al. (2009) and scaled by metallicity.

Emission lines are computed from the simulation on a cell-by-cell basis using the electron temperature, density, and ionization states predicted by RAMSES-RTZ. For UV and optical emission lines, we use PyNeb (Luridiana, Morisset & Shaw 2015) to compute emissivities and adopt atomic data from CHIANTI Version 10.1 (Dere et al. 2023) where possible. Otherwise we adopt the default atomic data in PyNeb. Each collisionally excited

² Note that by modeling our central source as a blackbody, we are over-predicting the number of ionizing photons of a typical O star with the same effective surface temperature. Nevertheless, these experiments are designed to be demonstrative of the qualitative trends for how turbulence impacts H II region emission lines.

TABLE 1
EMISSION LINE DIAGNOSTICS USED IN THIS WORK.

Name	Line Ratio	Diagnostic
$R_{\text{O II}}$	$[\text{O II}] \lambda 3728 / [\text{O II}] \lambda 3726$	n_e
$R_{\text{O III}}$	$[\text{O III}] 88\mu\text{m} / [\text{O III}] 52\mu\text{m}$	"
$R_{\text{S II}}$	$[\text{S II}] \lambda 6717 / [\text{S II}] \lambda 6731$	"
$R_{\text{S III}}$	$[\text{S III}] 33\mu\text{m} / [\text{S III}] 18\mu\text{m}$	"
$R_{\text{C III}}$	$[\text{C III}] \lambda 1906 / [\text{C III}] \lambda 1908$	"
$R_{\text{N II}}$	$[\text{N II}] 205\mu\text{m} / [\text{N II}] 122\mu\text{m}$	"
$R_{\lambda 4363}$	$[\text{O III}] \lambda 4363 / [\text{O III}] \lambda 5007$	T_e
$R_{\lambda\lambda 3727}$	$[\text{O II}] \lambda 3727 / [\text{O II}] \lambda\lambda\lambda\lambda 7320, 7330$	"
$R_{\lambda 3726}$	$[\text{O II}] \lambda 3726 / [\text{O II}] \lambda\lambda\lambda\lambda 7320, 7330$	"

line is modeled with 15 energy levels. We also consider mid-IR and far-IR emission lines. These are computed as in RAMSES-RTZ for cooling with a method that closely follows CLOUDY (Ferland et al. 2017).

A full list of all diagnostics used in this work for electron density and temperature is provided in Table 1, while the method of inferring metallicities is described in Section 2.1.3.

2.1.1. Density

As described, electron density can be inferred from closely-spaced doublet states that have different critical densities. We show in Figure 1 six line ratios measured from the homogeneous simulations as a function of density for the five metallicities. For comparison, we show the theoretical values for these line ratios as computed with PyNeb assuming a temperature of 10^4 K. In general, we find that these diagnostics follow the expected relations. Furthermore, we confirm that the curves traced by ratios of IR lines show an added metallicity dependence as predicted by Kewley et al. (2019), with lower metallicity realizations producing a decreased ratio at lower electron number densities.

2.1.2. Temperature

Unlike density³, temperature is not constant within the Strömgren sphere. Models with different metallicities can exhibit temperature gradients, either positive or negative, depending on metallicity (e.g. Garnett 1992; Stasinska 2005). For this reason, when referring to temperature, we adopt the “line” temperature, defined by Stasinska (1978) as:

$$\epsilon_\lambda(T_{\text{line}}) = \frac{\int n_X n_e \epsilon_\lambda(T) dV}{\int n_X n_e dV}, \quad (1)$$

where n_X is the number density of the ionic species. T_{line} represents the temperature which when evaluating the emissivity of a line gives the volume-averaged emissivity weighed by the electron and ion number densities. This temperature is useful because when used to calculate metallicity with a “direct” method, it gives the correct answer (e.g. Cameron, Katz & Rey 2023). When temperature is constant, the temperature measured from emission line ratios is the line temperature; however, if

³ In actuality, electron density is not exactly constant within the Strömgren sphere, particularly at the transition regions at the edge. This impacts ions like S II that can exist in both ionized and neutral gas more than others. Nevertheless, our models can be reasonably well approximated as having constant electron density within R_{S} .

a temperature distribution is present, T_{line} is not necessarily that measured from an emission line ratio.

We show in Figure 2 the electron temperature as measured from the $R_{\lambda 4363}$ ratio for each of five metallicities and various densities as a function of T_{line} . For guidance, we show theoretical values computed with atomic data produced from PyNeb, assuming an electron density of 300 cm^{-3} . Overall, within the homogeneous H II regions, the temperature diagnostic works reasonably well despite small variations in temperature. The “ratio temperature” well-matches the line temperature for $[\text{O III}] \lambda 4363 / \lambda 5007$, which is key for the metallicity estimates we discuss below.

2.1.3. Metallicity

Oxygen abundance (metallicity) is calculated using the direct T_e method. We use the ratio of auroral lines to other forbidden collisionally excited lines to measure the electron temperature (ratio temperature). This temperature is then used to infer the emissivities of the observed emission lines. The oxygen abundance is estimated as

$$\begin{aligned} \frac{\text{O}}{\text{H}} &\approx \frac{\text{O}^+}{\text{H}^+} + \frac{\text{O}^{++}}{\text{H}^+} \\ &= \frac{L_{\lambda\lambda 3727}}{L_{\text{H}\beta}} \frac{\epsilon_{\text{H}\beta}(T)}{\epsilon_{\lambda\lambda 3727}(T)} + \frac{L_{\lambda 5007}}{L_{\text{H}\beta}} \frac{\epsilon_{\text{H}\beta}(T)}{\epsilon_{\lambda 5007}(T)}. \end{aligned} \quad (2)$$

This equation is a relatively good approximation because the first ionization states of O and H are strongly coupled due to charge exchange reactions and as a result of the high energy required to ionize O to O^{3+} , the abundance of O^{3+} is negligible in stellar-dominated H II regions to an extent where it can be safely ignored for metallicity calculations (Berg et al. 2021). We note that the temperatures that enter the emissivity calculation need not be the same. This is discussed further below.

2.2. Turbulent Boxes

Having confirmed that our constant density models reproduce the expected behaviour between emission line luminosity and temperature/density, here we consider the impact of a turbulent density field on the same emission line diagnostics. The numerical setup is nearly identical to the homogeneous simulations apart from the density distribution.

To generate turbulent initial conditions, we start with the homogeneous volume with density of 300 H cm^{-3} in a 10 pc box with spatial resolution of 0.039 pc. We then drive turbulence with a mach number of 5.5 and a natural mixture of compressive to solenoidal modes (see e.g. Federrath et al. 2010). The turbulence is modeled using a Ornstein-Uhlenbeck process (e.g. Eswaran & Pope 1988; Federrath et al. 2010) as implemented in RAMSES (see details in Brucy et al. 2024). We adopt a parabolic forcing spectrum for the turbulence which is injected on scales of $1L_{\text{box}} - \frac{1}{3}L_{\text{box}}$. We first let the turbulence develop for a few autocorrelation timescales and then we output the density field every autocorrelation timescale for ten cycles. This provides us ten realizations of a turbulent density field for each metallicity. For each output, we freeze the density field, inject the same O-star at the center of the box, and evolve the radiation field until the simulation reaches a steady-state. We consider metallicities between 5% and 100% of solar (i.e. excluding the

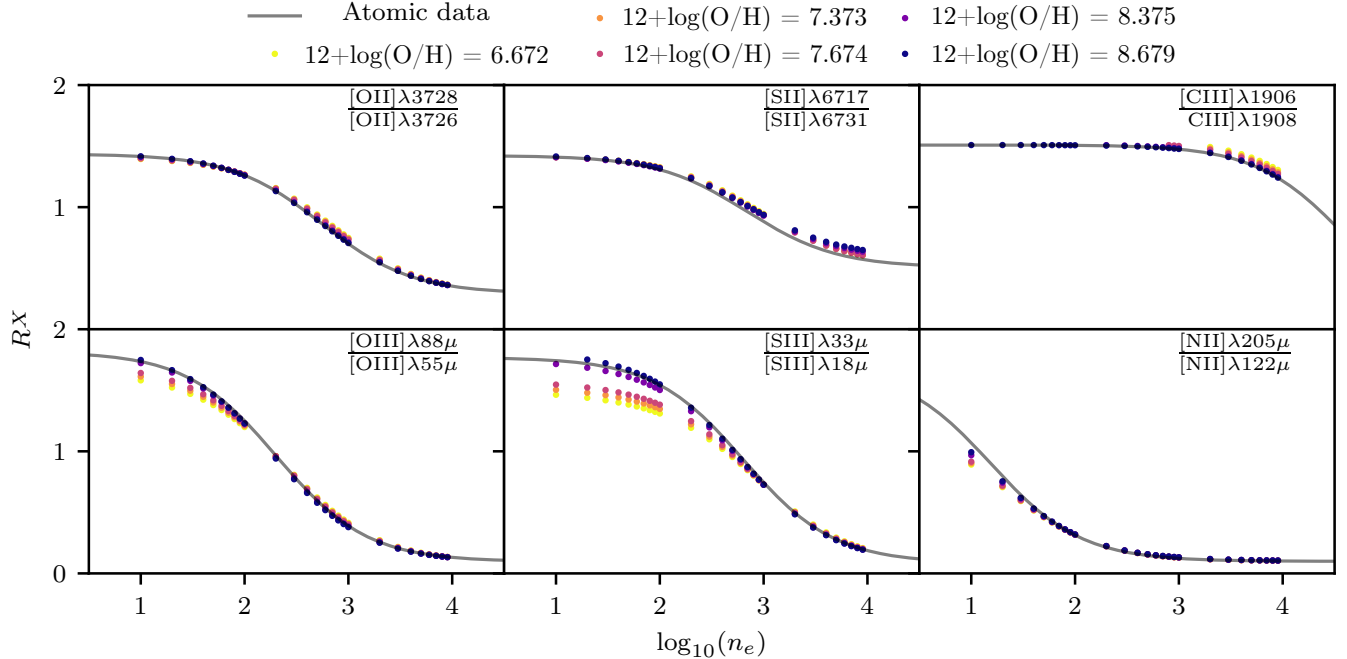


FIG. 1.— Normalized emission line ratio diagnostics as a function of electron density for each of the homogeneous boxes coloured by their metallicity. The smooth curves show the predicted ratio for a uniform electron temperature of 10^4 K.

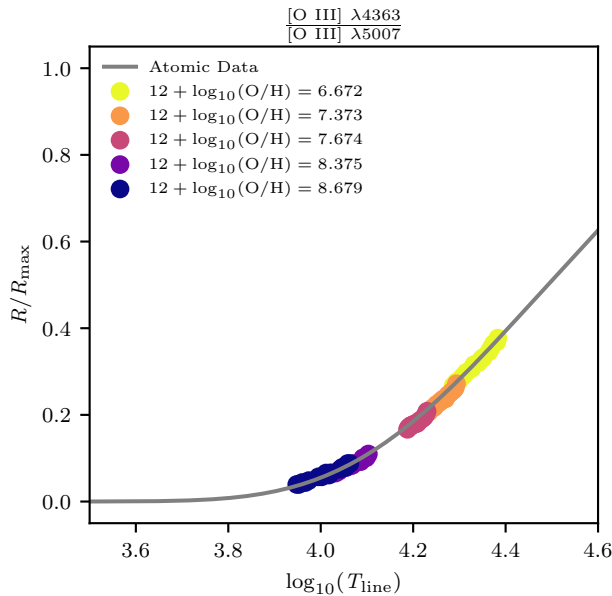


FIG. 2.— Normalized $R_{\lambda 4363}$ metallicity diagnostic as a function of line temperature (defined by Equation 1) for each of the homogeneous boxes colored by their metallicity. The curve shows the predicted ratio for a uniform electron number density of 300 cm^{-3} .

lowest metallicity used in the homogeneous simulations). Because of the finite box size and the complex density field that is well represented by a lognormal PDF, the escape fraction of ionizing photons is > 0 in some realizations, but typically remains below 10%.

In Figure 3 we show maps of a density slice, a column density map, a temperature slice, an integrated O II map, an O II slice, and an integrated O III map for one of the

turbulent realizations. Within the slice, the density can vary by four orders of magnitude while the temperature varies by up to $\sim 5,000$ K. The shape of the H II region is complex and is traced by O II, while O III fills the medium by volume. These properties are representative of all of the turbulent simulations, independent of metallicity.

Jin, Kewley & Sutherland (2022b) recently showed that in a turbulent medium, emission lines that trace the edge of the ionization fronts (i.e. [N II] and [O II]) tend to increase in luminosity compared to a homogeneous medium of the same mean density while volume filling emission lines (e.g. [O III]) tend to decrease. Our simulations show the exact same behaviour. In Figure 4 we show the ratios of [O III]/H β , [N II]/H α , and [O III]/[O II] for the constant density simulations (orange points) compared with the turbulent realizations (blue points with error bars). We see systematic differences between the homogeneous simulations and the turbulent volumes at the same mean density where [O III]/H β decreases, [N II]/H α increases and [O III]/[O II] decreases, consistent with Jin, Kewley & Sutherland (2022b). These shifts are not insignificant, in the case of [O III]/[O II], the change can be as much as a factor of two while for the other ratios, the variation can be up to $\sim 40\%$. The exact amount that a line ratio varies is sensitive to the type of turbulence (both mach number and compressive to solenoidal ratio), and this will be explored in future work.

As Jin, Kewley & Sutherland (2022b) point out, the likely physical origin of the enhancement in emission from boundary species is due to the surface area of the ionization front being enhanced by the complex density field. Likewise, most of the nebula by volume is at lower density than the mean which may suppress emission from

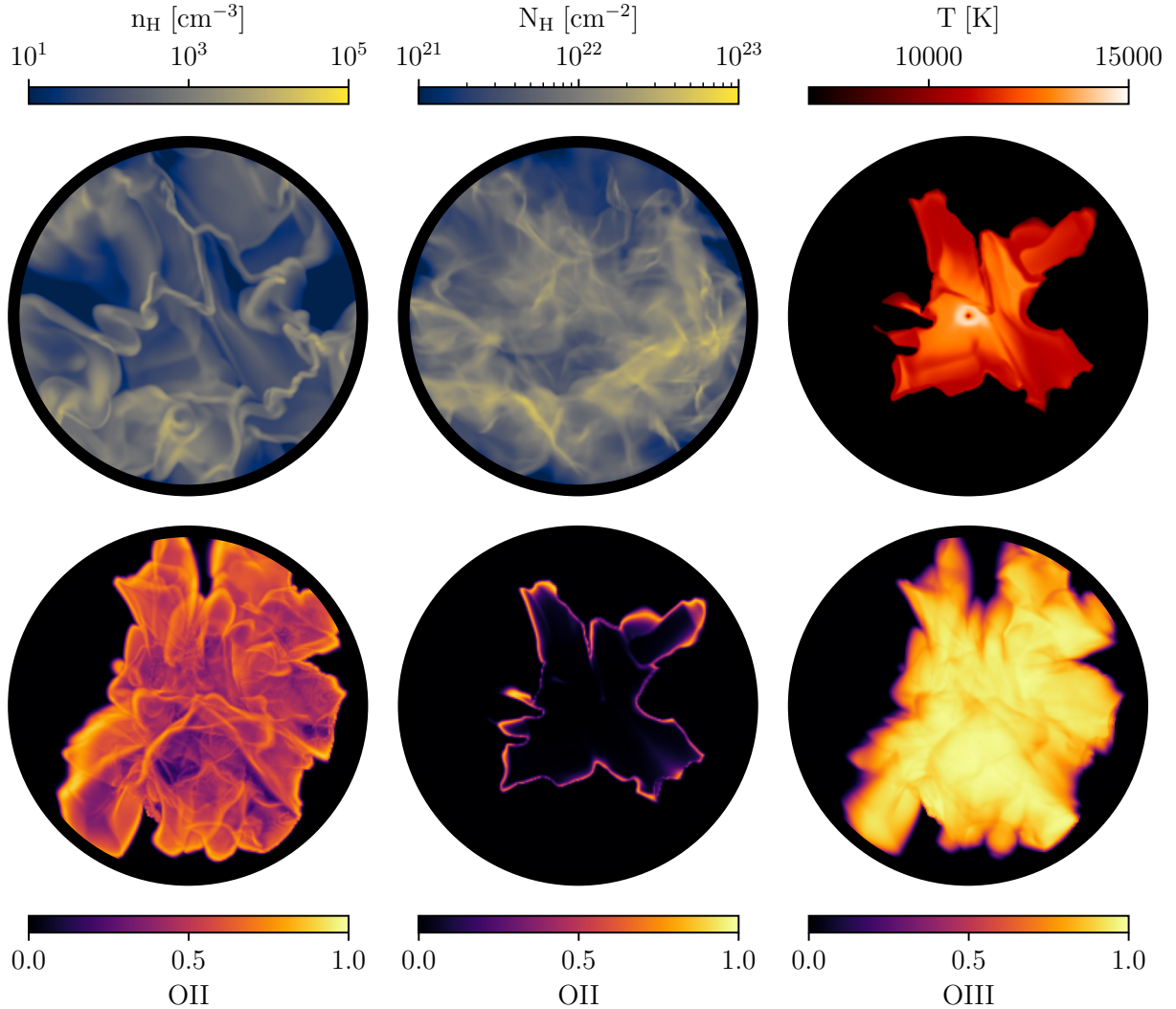


FIG. 3.— Top row, from left to right: hydrogen density slice, hydrogen column density map, temperature slice. Bottom row, from left to right: integrated O II map, O II slice, integrated O III map. The diameter of each panel is 10 pc.

the volume filling species.

Stated more rigorously, the luminosity of an emission line is proportional to both density and volume such that $L \propto n_{\text{ion}} n_e V$, where n_{ion} is the number density of the relevant ion (e.g. O⁺, O⁺⁺, N⁺, etc.), n_e is the electron number density, and V is the volume of the H II region. In the case of pure hydrogen, in a homogeneous medium, the density dependence divides out and the luminosity of the Balmer lines goes as $L \propto Q$, where Q is the emission rate of ionizing photons per second. In principle, the hydrogen recombination lines act as a photon counter and the same should be true in the case of the turbulent H II regions, which is why we see little variation in their luminosities. However, the same is not true for the other strong collisionally excited metal lines that we consider. The strength ionization parameter at the Strömgren radius partially dictates the size of the transition layer between ionized and neutral gas. If the surface area of the H II region increases, simply by conservation of pho-

tons, the average ionization parameter at the transition layer must decrease. Lowering the ionization parameter increases the size of the transition layer which would increase the emission from the boundary species. For large enough density contrasts, the H II region should preferentially terminate in higher density gas which would also decrease U .

Our results have clear importance for interpreting observations because [O III]/H β is commonly used as a metallicity diagnostic, the combination of [O III]/H β and [N II]/H α can differentiate between different types of ionization sources, while [O III]/[O II] is considered to trace ionization parameter. Systematic changes in these line ratios due to complex density structure would bias the interpretation of observed spectra. This is demonstrated in Figure 5 where we show our homogeneous and turbulent models on the classic BPT (Baldwin, Phillips & Terlevich 1981) and VO (Veilleux & Osterbrock 1987) diagrams with respect to local SDSS galaxies and high-

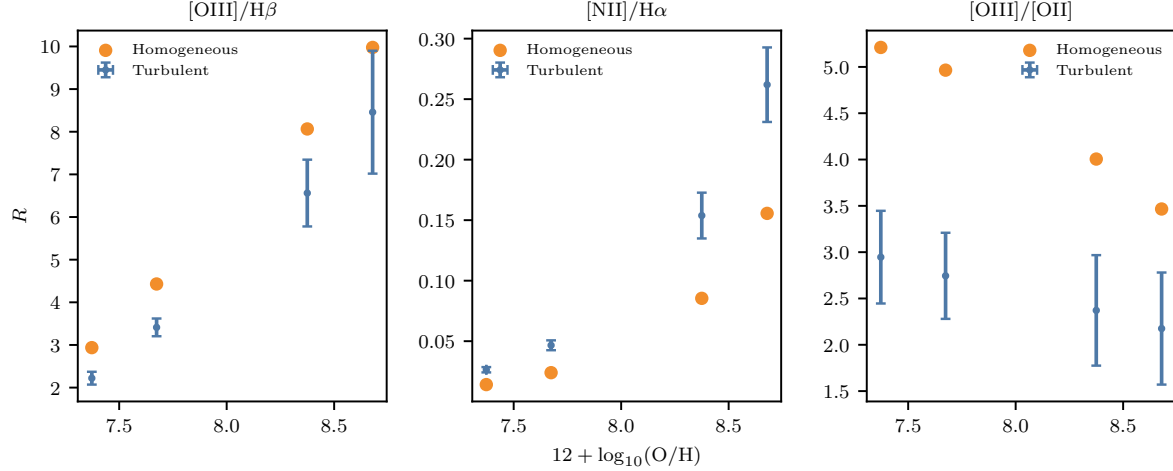


FIG. 4.— Comparison of diagnostic emission-line ratios from the homogeneous and turbulent simulations as a function of metallicity. $[\text{O III}]/\text{H}\beta$, $[\text{N II}]/\text{H}\alpha$, and $[\text{O III}]/[\text{O II}]$ are showed in the left, center, and right, respectively. Orange points represent data from homogeneous simulations. Each blue point represents the average across 10 turbulent realizations, with error bars indicating the standard deviation.

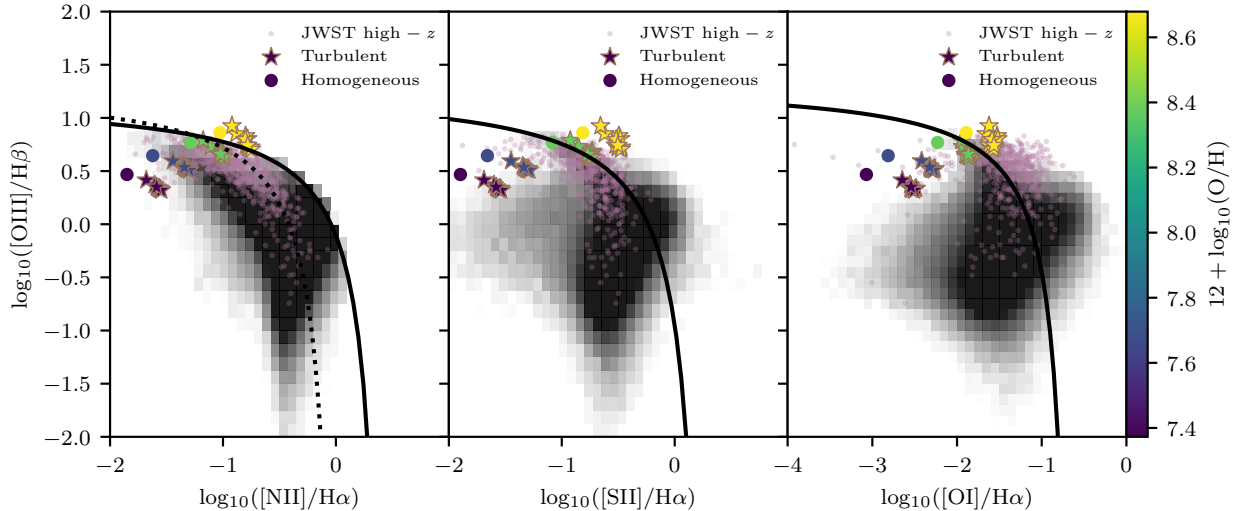


FIG. 5.— Comparison of diagnostic emission-line ratios from the homogeneous and turbulent simulations with observational data. The left panel shows $\log_{10}([\text{N II}]/\text{H}\alpha)$ vs. $\log_{10}([\text{O III}]/\text{H}\beta)$, the center panel shows $\log_{10}([\text{S II}]/\text{H}\alpha)$ vs. $\log_{10}([\text{O III}]/\text{H}\beta)$, and the right panel shows $\log_{10}([\text{O I}]/\text{H}\alpha)$ vs. $\log_{10}([\text{O III}]/\text{H}\beta)$. Small purple dots represent high redshift galaxies from the DAWN JWST Archive (Brammer & Valentino 2025). Homogeneous simulations are the larger dots and turbulent simulations are the brown-outlined stars. Both are colored by metallicity. The background gray histogram indicates the number density of galaxies from the Sloan Digital Sky Survey (SDSS, Aihara et al. 2011). The solid lines in each panel represent relations from Kewley & Dopita (2002) to separate star-forming galaxies/H II regions from AGN. The dashed line in the first panel is the empirical discriminator Kauffmann et al. (2003). AGN are filtered out according to the Kewley & Dopita (2002) relation for $\log_{10}([\text{N II}]/\text{H}\alpha)$ vs. $\log_{10}([\text{O III}]/\text{H}\beta)$.

redshift JWST observations. Indeed, the turbulent models, for a fixed mean density and metallicity, can span a significant region of parameter space.

Additionally, we see that turbulence causes a non-negligible shift in how we interpret the theoretical calibrations for total excitation and ionization parameter. This is shown in Figure 6, where we compare R23, an indicator of total excitation, to O32, a tracer for ionization parameter (e.g. Kewley et al. 2019). We see that turbulence causes up to a 0.4 dex decrease in O32 and up to a 0.1 dex decrease in R23. Hence, a highly turbulent medium would typically be inferred to have lower ionization and excitation.

Having shown that the emission line ratios fundamen-

tally change due to geometry, below we consider how a complex turbulent geometry impacts inferences of density, temperature, and metallicity.

3. INFERRING DENSITY, TEMPERATURE, AND METALLICITY FROM TURBULENT H II REGIONS

3.1. Temperature

Before we can infer the metallicity of the turbulent H II regions, it is crucial to consider the variety of electron temperatures that can be used in T_e -based metallicity measurements. Following the standard two-zone approximation (Garnett 1992), we assume separate electron temperatures for the boundary-tracing O II

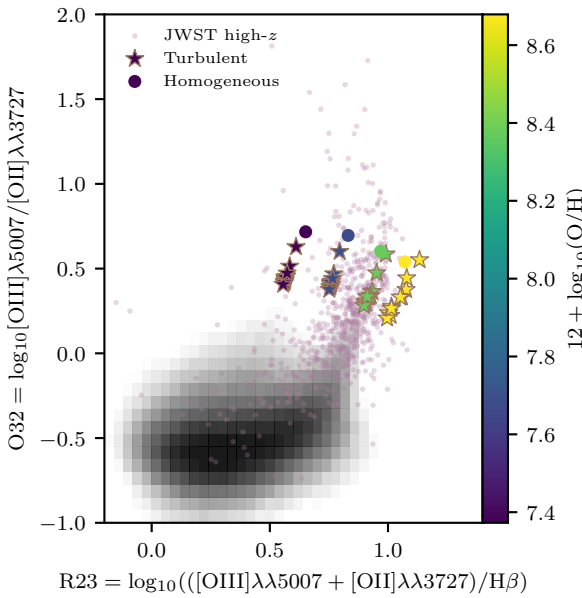


FIG. 6.— Comparison of O32 versus R23 from the homogeneous and turbulent simulations with observational data. Note that $[\text{O III}] \lambda\lambda 5007$ denotes the O III nebular doublet consisting of $[\text{O III}] \lambda 4959$ and $[\text{O III}] \lambda 5007$, and $[\text{O II}] \lambda\lambda 3727$ denotes the O II doublet consisting of $[\text{O II}] \lambda 3726$ and $[\text{O II}] \lambda 3729$. Purple dots represent high redshift galaxies from the DAWN JWST Archive (Brammer & Valentino 2025). Homogeneous simulations are represented by large circles and turbulent simulations are the brown-outlined stars, with each colored by metallicity. The background gray histogram indicates the number density of galaxies from the Sloan Digital Sky Survey (SDSS, Aihara et al. 2011).

zone and volume-filling O III zone. To derive $T_{\text{O III}}$, we adopt the direct method approach of utilizing the ratio temperature of $[\text{O III}] \lambda 4363/\lambda 5007$ (Menzel, Aller & Hebb 1941). For $T_{\text{O II}}$, one of two separate approaches is generally employed in literature. When accurate measurements of O II auroral lines are available, $T_{\text{O II}}$ is measured using the O II auroral lines. Otherwise, it is derived by assuming a theoretically or empirically determined relation between $T_{\text{O II}}$ and $T_{\text{O III}}$ (e.g. Campbell, Terlevich & Melnick 1986; Garnett 1992). To account for the different approaches, we experiment with four separate estimation schemes of $T_{\text{O II}}$.

1. $T_{\text{O II}} = T_{\text{O III}}$: an approximation that effectively adopts a one-zone approach.
2. The direct $T_{\text{O II}}$ method using $R_{\lambda\lambda 3727}$: the typical approach of estimating $T_{\text{O II}}$ to be the ratio temperature of the O II auroral quadruplet to the strong O II doublet (Pérez-Montero & Díaz 2003).
3. The direct $T_{\text{O II}}$ method using only $[\text{O II}] \lambda 3726$: nearly identical to method two, except only considering the strong O II line with the higher critical density. In doing so, we aim to reduce the effect of density inhomogeneities on the line ratio.
4. $T_{\text{O II}} = 0.7T_{\text{O III}} + 0.3$: a widely adopted theoretical relation from Campbell, Terlevich & Melnick (1986), based on models of Stasinska (1982).

In addition, we repeat the use of Method 2 to infer T_e and metallicity for the homogeneous simulations, establishing a baseline of comparison for the effects of turbulence.

Figure 7 shows that across all turbulent realizations, our inferred values of $T_{\text{O II}}$ are systematically higher than the line temperature. The magnitude of deviation and scatter increase with lower metallicity / higher $T_{\text{O III}}$. Correspondingly, our inferred $T_{\text{O II}} - T_{\text{O III}}$ relations are much steeper than the relation between the O II line temperature and $T_{\text{O III}}$.

3.2. Metallicity

With $T_{\text{O II}}$ and $T_{\text{O III}}$ determined, we compute direct-method metallicities using Equation 2. We adopt various $T_{\text{O II}}$ to calculate the emissivity ratio of $\text{H}\beta$ and $[\text{O II}] \lambda\lambda 3727$ and the direct $T_{\text{O III}}$ to calculate the emissivity ratio of $\text{H}\beta$ and $[\text{O III}] \lambda 5007$. We note that electron density also affects the value of emissivity and therefore adopt the density value measured from the $R_{\text{O II}}$.

Figure 8 shows that across all turbulent realizations, our inferred metallicities deviate from the true values by $0.02 - 0.1$ dex, with typical offsets closer to 0.05 dex. The scatter increases with metallicity. Different assumptions on $T_{\text{O II}}$ introduce < 0.05 dex of scatter into the inferred metallicity, which is a smaller effect than the presence of turbulence. The metallicites we infer from the turbulent realizations are always systematically below those we infer from the homogeneous realizations, which differ from true metallicity values by < 0.02 dex regardless of metallicity. This implies that turbulence does indeed systematically bias direct method metallicity estimates.

Of the four approaches of estimating $T_{\text{O III}}$, the Campbell, Terlevich & Melnick (1986) relation yields the most accurate estimates at all metallicities. For low-metallicity realizations, the second and third variations ($R_{\lambda\lambda 3727}$ and $R_{\lambda 3726}$) outperform the simple $T_{\text{O II}} = T_{\text{O III}}$ approximation, but the opposite trend holds at high metallicites. Furthermore, using $R_{\lambda 3726}$ consistently yields more accurate results, although the difference is < 0.01 dex and generally not statistically significant.

However, it is worth noting that the choice of $T_{\text{O II}}$ affects our metallicity estimates by at most 0.05 dex, likely due to the fact that the overall mass of O^{++} is greater than that of O^+ by a factor of $\sim 2 - 3$ (depending on metallicity). As seen in Figure 7, our estimates of $T_{\text{O II}}$ can differ with respect to each other by $> 2,000$ K, and yet the estimates of metallicity still remain within 0.05 dex of each other. For lower ionization parameters, we can expect the choice of $T_{\text{O II}}$ to have a much more significant effect on the direct method estimate of metallicity. The choice of how one calculates $T_{\text{O II}}$ is therefore likely more important in the lower redshift Universe where ionization parameters tend to be lower.

3.3. Density

Having quantified the discrepancy between T_e -derived metallicities and the true metallicity of the simulated H II regions, we now consider the electron density. However, for the case of electron density, the question of which “true” electron density we should recover is nontrivial. For photoionization models simulated at constant density, such as our homogeneous models, the electron den-

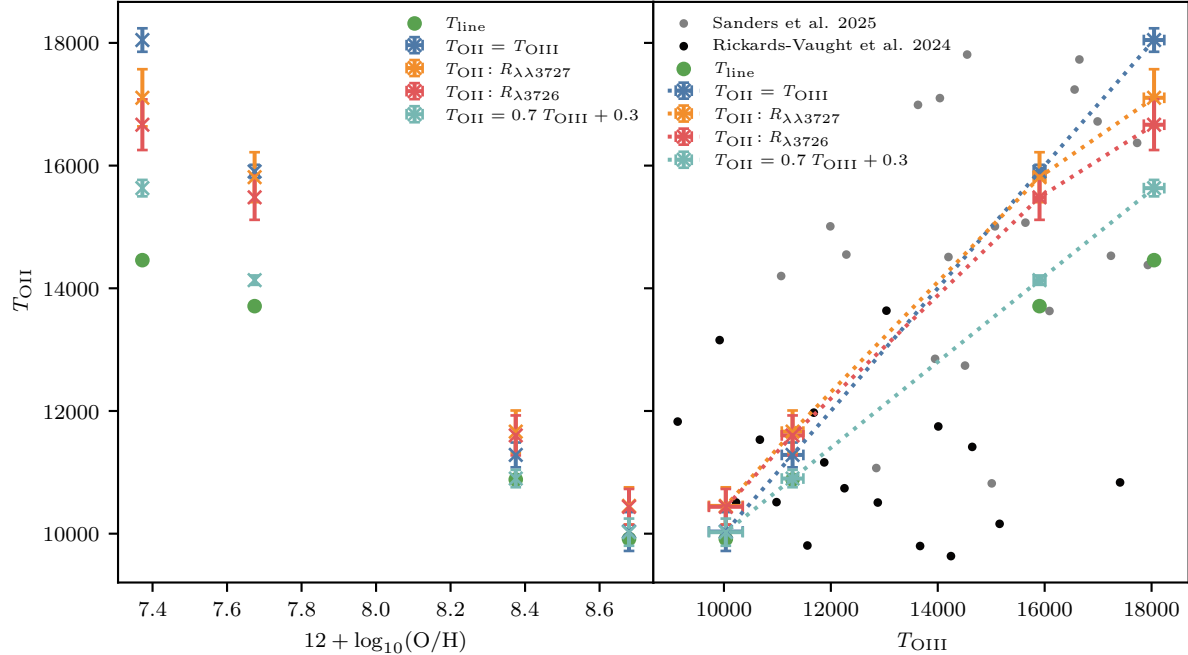


FIG. 7.— (Left) Comparison of $T_{\text{O II}}$ values measured from four different approaches of the direct method to the [O II] line temperature defined by Stasinska (1978). Green dots represent the line temperature at each metallicity, and the colored \times -marks represent the values of $T_{\text{O II}}$ obtained using the different approaches. Each turbulent data point represents the mean of measured metallicities from 10 realizations of the same metallicity, with error bars indicating the standard deviation. (Right) Comparison of $T_{\text{O II}}$ and $T_{\text{O III}}$ for turbulent simulations at 4 metallicities. Here, $T_{\text{O III}}$ is measured using the $R_{\lambda 4363}$ line ratio and $T_{\text{O II}}$ is measured using the 4 methods outlined in Section 3 and plotted as \times -marks that are color coded accordingly. The O II line temperatures as defined in Equation 1 of simulations of each metallicity are plotted as green dots. Each turbulent data point represents the mean of measured metallicities from 10 realizations of the same metallicity, with error bars indicating the standard deviation. We provide comparisons with similarly-derived observational data from local H II regions (Vaught et al. 2024) (black dots) and high redshift JWST data (Sanders et al. 2025) (gray dots).

sity remains constant in the fully ionized regions⁴. Alternatively, both empirically and theoretically, one may expect density stratification in a nebula (Stasinska 1978; Garnett 1992; Wang et al. 2004). In the top panel of Figure 9 we show an electron density histogram of the $0.05 Z_{\odot}$ turbulent simulations. We see that the volumetric mean density of the homogeneous simulations is $\sim 300 \text{ cm}^{-3}$, while the volumetric mean density of the turbulent simulations is $\sim 100 \text{ cm}^{-3}$. Additionally, we see that turbulence causes electron density to scatter between $10 - 500 \text{ cm}^{-3}$ and extend to densities 3000 cm^{-3} , confirming the presence of density variations. As a result of this, we expect density diagnostics relying on different parent ions to probe different parts of the H II region and provide different values of electron density. Taking this into account, we compare the values of electron density measured from our calibrated density diagnostics with the mass-weighted density of the parent ion as well as the luminosity-weighted densities of the emission lines used in the diagnostic. In doing so, we find that neither the mass-weighted densities of the parent ions nor the initial/final volumetric mean density of the H II region are accurately probed by the density diagnostics.

As shown in Figure 10, all diagnostics except $R_{\text{N II}}$ systematically overestimate the mass-weighted densities. Typical offsets range from 100 to 300 cm^{-3} ($\sim 30 - 50\%$ higher), reflecting the fact that line emission is dispropor-

tionately biased toward the denser parts of the H II regions. In contrast, the diagnostics are generally in agreement (to within 100 cm^{-3}) with the luminosity-weighted density of the emission line with the lower critical density, with the exception of $R_{\text{O II}}$, $R_{\text{N II}}$, and $R_{\text{C III}}$. We note that two of these exceptions can be excluded for physical reasons. $R_{\text{N II}}$ consistently overestimates the mass-weighted densities and $R_{\text{C III}}$ shows no consistent trend and significant scatter. Both effects can be traced to the fact that their mass-weighted densities fall outside the density-sensitive regimes of the line-ratios (Figure 11), making them highly sensitive to small fluctuations. Furthermore, although variations in the temperature used to calibrate density diagnostics (typically 10^4 K) alters the density-sensitive regimes of line-ratios by negligible amounts, their effect on the density-insensitive regimes of line-ratios are significant. We assume a uniform temperature of 10^4 K for all of our temperature diagnostics, which inevitably deviates from the electron temperature characteristic of each ionization zone. As such, the trends we find that pertain to $R_{\text{N II}}$ and $R_{\text{C III}}$ are not reflective of the trends that should pertain to density diagnostics.

4. DISCUSSION

In this section, we discuss the underlying physics behind the trends found in Section 3. In addition, we contextualize the magnitude of the effects of turbulence in relation to the relevant literature and identify future research directions.

⁴ Note that it can decrease in partially ionized gas.

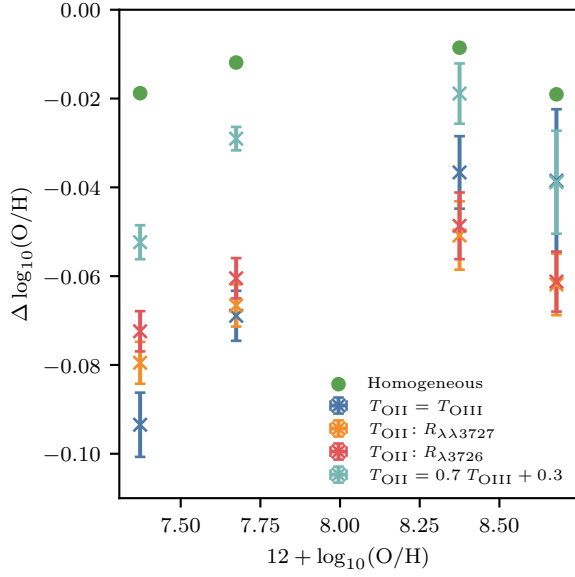


FIG. 8.— Comparison of the offset between the true metallicity of simulations and measured metallicities. Metallicity was measured for the homogeneous and turbulent realizations, with the green dots representing the homogeneous simulations and the colored \times -marks representing the turbulent realizations. Four different approaches were taken to measure metallicity for the turbulent realizations, with the only difference being the method of estimating the value of $T_{O\text{ II}}$ to be utilized in Equation 2. Each turbulent data point represents the mean of measured metallicities from 10 realizations of the same metallicity, with error bars indicating the standard deviation.

4.1. Abundance Discrepancy Problem

Several studies have shown gas-phase metallicities derived from the direct T_e method are systematically lower than those derived from recombination line (RL) methods by ≥ 0.2 dex, the abundance discrepancy problem (Esteban et al. 2004; Garcia-Rojas & Esteban 2007). Our simulations indicate that even in the presence of supersonic turbulence, the direct method recovers true metallicity values to within 0.1 dex, as long as the mach number remains below ~ 5.5 . We verified that applying RL methods to our simulations result in more accurate metallicity measurements than direct method-derived metallicites; as such, turbulence alone does not seem to account for the entire abundance discrepancy factor (ADF).

Several explanations have been proposed for the ADF, including temperature fluctuations (e.g. Peimbert 1967; Esteban et al. 2002; Peimbert & Peimbert 2013), chemical inhomogeneities (Yuan et al. 2010), and non-Maxwellian electron distributions such as κ distributions (Nicholls, Dopita & Sutherland 2012). Nevertheless, our results show that the complex internal structures driven by turbulence do in fact result in systematic underestimates in direct method metallicities. And although our simulations do not fully recover the ADF found in observational studies, they confirm the role turbulence plays in affecting metallicity and electron temperature diagnostics.

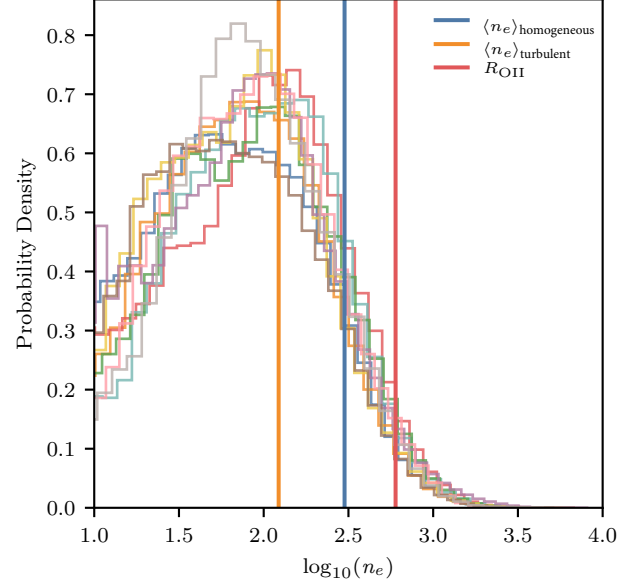


FIG. 9.— (Top) Electron density PDF of the $0.05 Z_{\odot}$ simulations. The volumetric mean density of homogeneous simulations, mean volumetric mean density of turbulent simulations, and the $R_{O\text{ II}}$ line-ratio derived density are labeled using blue, orange, and red vertical lines, respectively. (Bottom) Cumulative distribution functions of emission line luminosity as a function of electron density for all lines used in this work for the same $0.05 Z_{\odot}$ model averaged over the ten realizations. Here we see that the luminosity is always dominated by gas above the mean volumetric density.

4.2. Discrepancy between $T_{O\text{ II}}$ Approaches

We found that inferring $T_{O\text{ II}}$ using $R_{\lambda\lambda 3727}$, which in theory should be more accurate, does not outperform the theoretical Campbell, Terlevich & Melnick (1986) relation, and for higher metallicities, also does not outperform the one-zone approximation. As seen in Figure 7, the relation of $T_{O\text{ II}} - T_{O\text{ III}}$ we obtain while using $R_{\lambda\lambda 3727}$ coincides far more closely to the simplistic one-zone approximation as opposed to the relation between

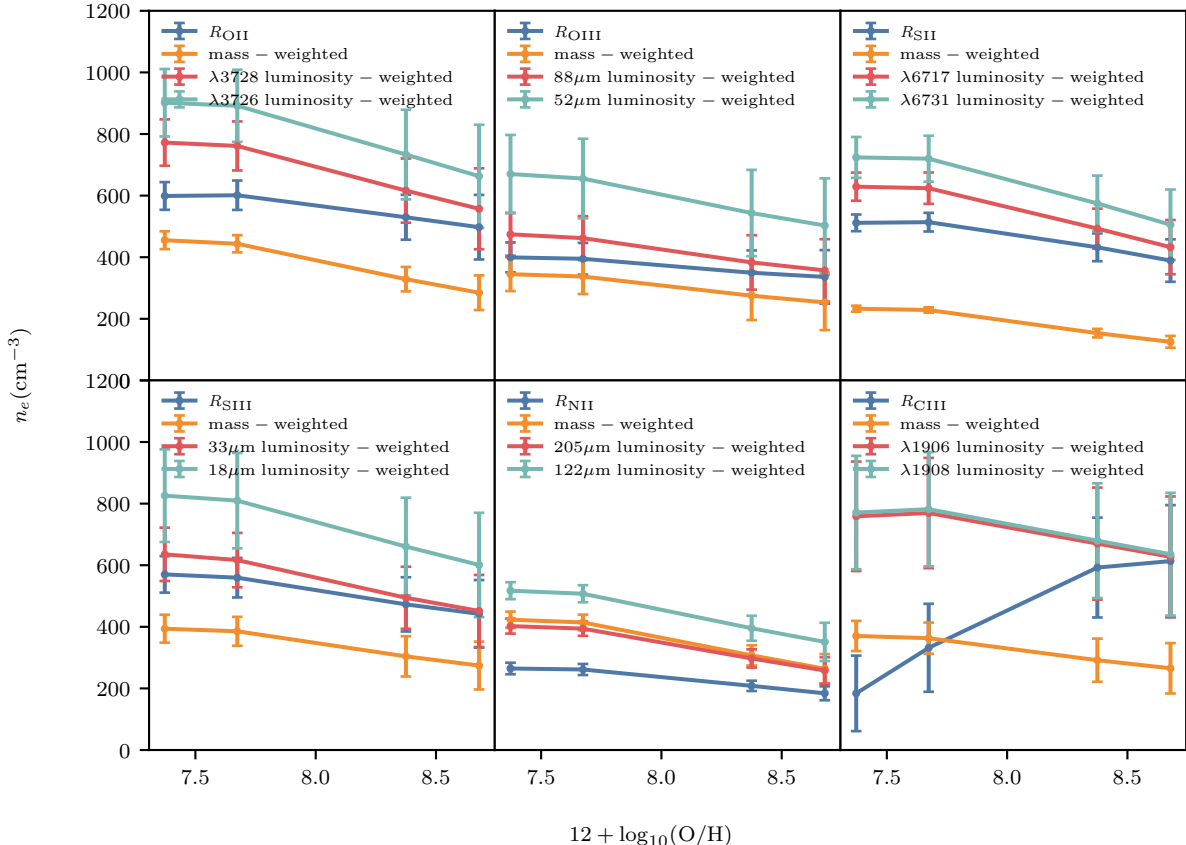


FIG. 10.— Comparison of emission-line-derived densities (blue) using $R_{O\text{ II}}$, $R_{O\text{ III}}$, $R_{S\text{ II}}$, $R_{S\text{ III}}$, $R_{N\text{ II}}$, $R_{C\text{ III}}$ at different metallicities. Additionally, each emission-line-derived metallicity is plotted against the mass-weighted electron density (orange) of the ion corresponding to the line ratio and the luminosity-weighted electron densities (red and cyan, respectively) of the emission lines used to construct the line ratio.

the line temperatures of $T_{O\text{ II}}$ and $T_{O\text{ III}}$. This finding is surprising; however, we offer some potential explanations for this phenomena.

Firstly, H II regions have been known to exhibit isothermal conditions at certain metallicities. For example, in the models of Kewley et al. (2019) they find that the isothermal conditions apply at a metallicity of $12 + \log(O/H) \sim 8.23$. Thus, it is expected for the one-zone approximation to work well for H II regions with select metallicites, though this can vary depending on the exact conditions. In Figure 7, we observe this metallicity to be $12 + \log(O/H) \sim 8.7$ for our simulations. In contrast, as the metallicity of H II regions deviate significantly from 8.7, a stronger temperature gradient forms, leading to inaccuracies in the one-zone approximation. This is the result of two key physical mechanisms. First, higher metallicity leads to increased radiative cooling. This is particularly true in the regions dominated by O^{++} due to the efficiency of fine structure cooling. Second, the higher abundance of metals causes increased radiation hardening towards the outer edges of the H II region, which leads to stronger heating of the regions dominated by O^+ (Kewley et al. 2019). The balance between these two effects determines when isothermal conditions are reached. This clearly depends

on metallicity, density, and the shape of the radiation field.

Furthermore, studies have found that the density sensitive $[O\text{ II}] \lambda\lambda 3727$ doublet causes the $R_{\lambda\lambda 3727}$ line ratio to be affected by density inhomogeneities by a non-negligible amount (Vaught et al. 2024). This leads to over-estimations of $T_{O\text{ II}}$, which ultimately result in the systematic under-prediction of metallicity, coinciding with the finding of studies such as Choustikov et al. (2025). At high redshifts, a similar process likely impacts $T_{O\text{ III}}$ (Martinez et al. 2025). As shown in the previous section, removing the higher critical density $[O\text{ II}] \lambda 3729$ line does reduce the effects of density inhomogeneities by a marginal amount. The density used to calibrate the $R_{\lambda\lambda 3727}$ line ratio is itself not entirely accurate, as it is computed using $R_{O\text{ II}}$, which we have determined earlier to be overly biased towards the high density regions. All of these factors contribute to the systematic error in the estimation of $T_{O\text{ II}}$, ultimately leading to the consistent metallicity underestimate of ~ 0.06 dex.

Our results suggest that theoretical $T_{O\text{ II}} - T_{O\text{ III}}$ relations may outperform methods that utilize the O II auroral lines as a result of the density dependence of $[O\text{ II}] \lambda\lambda 3727$ (see Figure 7).

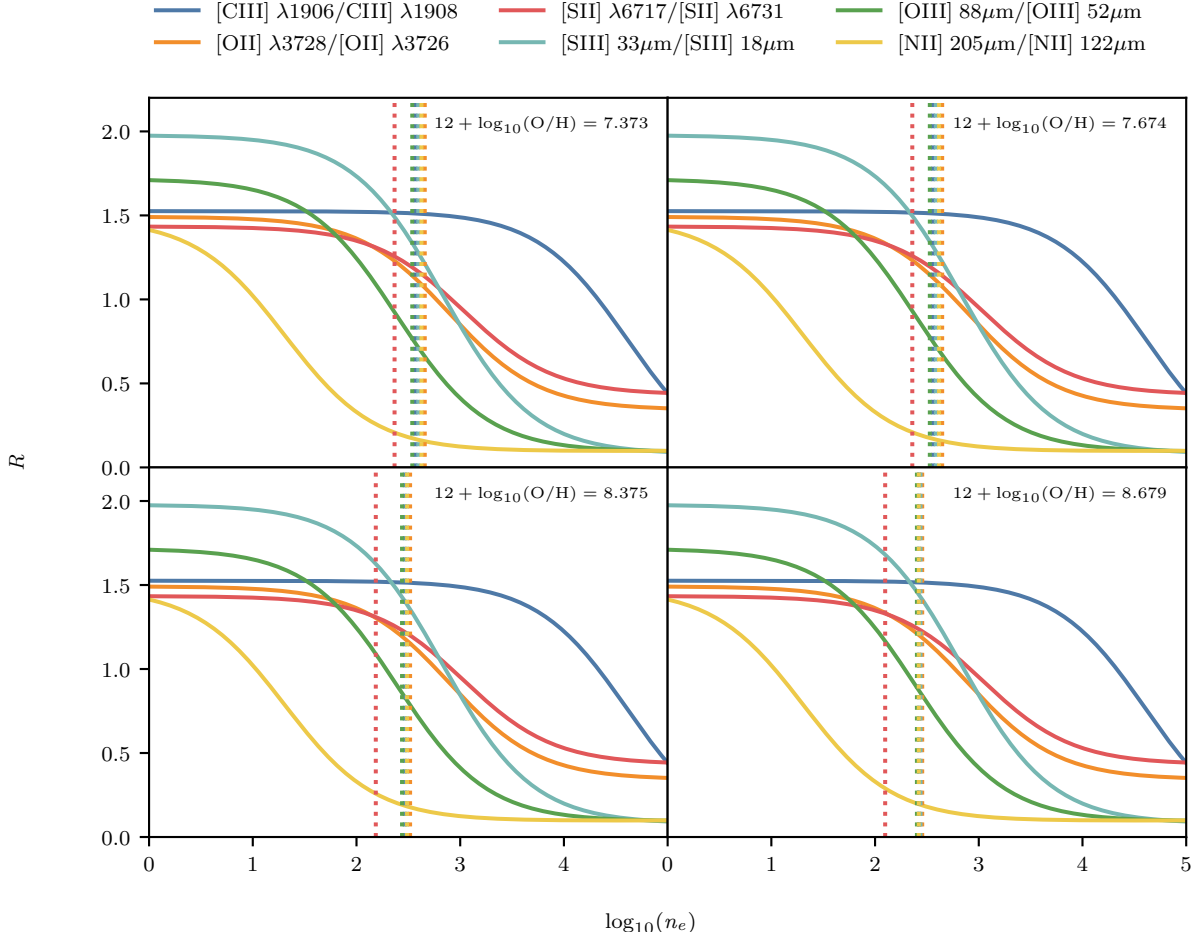


FIG. 11.— Line-ratio as a function of electron density for every density-sensitive diagnostic used in this work. For each metallicity, the mass-weighted electron densities of each ion (displayed in Figure 10) are marked with dotted vertical lines color coded with the same color of the line ratio diagnostic constructed using the corresponding parent ion.

4.3. Physical Interpretation of Inferred Densities in Turbulent H II Regions

Several studies have shown that applying constant density diagnostics to H II regions with complex density structures will recover values that are characteristic of the regions producing the most emission line strength as opposed to a volumetric-mean of the entire H II region (Kewley et al. 2019). Our results in the previous section are consistent with this finding, as we have shown that the electron density estimates inferred from the turbulent H II regions better reflect select luminosity-weighted densities as opposed to mass or volume-weighted densities. Specifically, we found that the line ratio densities align with the luminosity-weighted density of the lower critical density emission line of each density diagnostic.

The dominance of high density regions in line emission can be readily inferred from Figure 9. As mentioned in the previous section, the electron densities within the simulations extend to values as high as $\sim 3000 \text{ cm}^{-3}$. This high density tail is important because the emission line luminosity of a parcel of gas scales as n^2 (until the critical density of the line is reached). Thus even though the high density gas represents a small fraction of the mass and volume, it can contribute significantly to emission line luminosity. For example, although we

typically have $\sim 13 - 16 \times$ more gas cells with an electron density of 100 cm^{-3} compared to $\gtrsim 1000 \text{ cm}^{-3}$, the factor of ten difference in density in principle results in a factor of 100 difference in luminosity, which more than accounts for the relative sparsity of higher density gas parcels. There is nuance for individual lines in that as density changes, the ionization states may differ and once the critical density is reached, luminosity increases as n rather than n^2 . To explore this further, in the bottom panel of Figure 9 we show cumulative distribution functions of the luminosity of individual emission lines as a function of electron density averaged over the ten realizations of the $0.05 Z_\odot$ model. Indeed we find that the luminosity is always dominated by gas significantly denser than the mean volumetric density.

4.4. Discrepancy between Density Diagnostics

As described in the previous sections, studies have shown that density diagnostics relying on different parent ions probe different ionization zones within H II regions and thus recover different values of electron density (Wang et al. 2004; Méndez-Delgado et al. 2023). Figure 6 of Choustikov et al. 2025 has shown that this effect is very pronounced on galactic scales using cosmological simulations with a multi-phase ISM. However, it remains unclear how much the measured densities of dif-

ferent density diagnostics should differ from each other on the scale of individual H II regions. Nevertheless, we showed in previous sections that our inferred densities from diagnostics of different parent ions differ with each other by $\leq 200 \text{ cm}^{-3}$. As above, this result is certainly sensitive to the properties of the turbulence, which motivates running more simulations to systematically study a larger parameter space.

4.5. *Caveats*

Our turbulent H II regions are undoubtedly simplistic — they represent a first step beyond simple slab or spherical geometries that are nearly ubiquitous among published photoionization models. Our 3D setup is likely more physical than simple geometries, but still misses key physical effects that impact real H II regions. For example, the ISM is known to be turbulent (e.g. Larson 1981; Elmegreen & Scalo 2004), but the exact nature (compressive to solenoidal ratio, driving scale, power spectrum, mach number etc.) likely differs between environments. Transsonic and subsonic turbulence will produce emission line ratios more similar to the spherical models (Gray & Scannapieco 2017). We have specifically chosen a numerical setup where turbulence has an impact on the emission line ratios; however, our chosen parameters are unlikely to be representative of the ISM across different environments. A more systematic study varying the properties of the turbulence is warranted. Ideally one would even be able to infer the turbulence from the emission line ratios and their line shapes, but this is beyond the scope of our current work.

Arguably the most important assumption of our work is the exclusion of hydrodynamics. We placed a single O star at the center of numerous realizations of a turbulent gas density field and evolved them to ionization and thermal equilibrium. This assumption may be overly simplistic under two circumstances. First if the density is too low ($\lesssim 1 \text{ cm}^{-3}$), the timescale for the ionization front to reach the Strömgren radius becomes comparable than the lifetime of a massive O star. Implications of this are discussed in Katz et al. *in prep.*; however, in the context of this work, the box size is not large enough to capture this effect and thus the ionizing radiation leaks from the volume (i.e. $f_{\text{esc}} > 0$). Since f_{esc} is typically $< 10\%$, our results are not strongly impacted by leaking radiation. Second, in real H II regions, the gas is not static, but rather is sloshing around from turbulence, impacted by gravity, and subject to feedback from radiation pressure, photoheating, and stellar winds (e.g. Spitzer 1978; Draine 2011b; Klessen & Glover 2016). These effects are particularly important when the ionization front transitions from R-type to D-type. Moreover, depending on the medium, the radiation pressure or pressure from photoheating may circularize the H II region and drive a shell (e.g. Draine 2011a). In this case, a spherical H II region may be more appropriate than what we have assumed in our models. All of these effects motivate the need for simulations that self-consistently model the physics of star formation and stellar feedback in high-resolution, turbulent, magnetized molecular clouds (see e.g. Kimm et al. 2019; Grudić et al. 2021; Chon, Omukai & Schneider 2021; Kimm et al. 2022; Bate 2023; Menon et al. 2025). Work towards this end with RAMSES-RTZ is currently underway.

5. CONCLUSIONS

We have presented a suite of simulations at various metallicities designed to study the impact of density inhomogeneities driven by supersonic turbulence on density, temperature, and metallicity inferences from emission line ratios in static H II regions. Our work represents a step beyond the simple geometries of prior photoionization models, an assessment of how the physical condition of turbulence affects the efficacy of current nebular emission diagnostics. Our main results and conclusions are as follows:

1. Supersonic turbulence can drive significant systematic changes in strong emission line ratios when compared to homogeneous models of the same mean density. More specifically, we found $[\text{O III}]/\text{H}\beta$ decreases, $[\text{N II}]/\text{H}\alpha$ increases, and $[\text{O III}]/[\text{O II}]$ decreases, consistent with the fractal models of Jin, Kewley & Sutherland (2022b).
2. We compute the metallicities of homogeneous and turbulent simulations using multiple variations of the direct method (Figure 8). We show that turbulence leads to systematic underestimates of metallicity $< 0.1 \text{ dex}$. This deficit is less than the observationally determined abundance discrepancy factor of $> 0.2 \text{ dex}$ (Esteban et al. 2004; Garcia-Rojas & Esteban 2007).
3. We compare the values of metallicity and $T_{\text{O II}}$ determined using different variations of the direct method (Figure 7, 8). We find that the density inhomogeneities caused by turbulence affect methods that utilize the O II doublet to a larger extent than methods that utilize a theoretically determined $T_{\text{O II}} - T_{\text{O III}}$ relation.
4. We compare the electron density diagnostics to the mass-weighted electron density of the corresponding parent ion and luminosity-weighted electron density of the corresponding emission lines (Figure 10). In agreement with previous studies (Kewley et al. 2019), we find that diagnostic-derived electron densities are a poor tracer of the volumetric mean electron density of an H II region or the mass-weighted electron density of any given ion. They instead align closely with the luminosity-weighted density of the lower critical density line used in the diagnostic.

Our numerical implementation of turbulence, remains an important first step towards the development of more complex, realistic photo-ionization models. The magnitude by which turbulence can impact observed emission line ratios motivates the need for more complex models of H II regions.

ACKNOWLEDGMENTS

We thank the referee for their constructive comments on the manuscript. The authors thank Romain Teyssier for both developing and open-sourcing RAMSES.

This work made extensive use of the dp265 and dp016 projects on the DiRAC ecosystem. HK is particularly grateful to Christopher Mountford and Alastair Basden for support on DIAL3 and Cosma8, respectively.

HK is especially thankful for the support on Glamdring provided by Jonathan Patterson. The material in this manuscript is based upon work supported by NASA under award No. 80NSSC25K7009. AJC gratefully acknowledges support from the Cosmic Dawn Center through the DAWN Fellowship. The Cosmic Dawn Center (DAWN) is funded by the Danish National Research Foundation under grant No. 140.

This work used the DiRAC@Durham facility managed by the Institute for Computational Cosmology on behalf of the STFC DiRAC HPC Facility (www.dirac.ac.uk).

The equipment was funded by BEIS capital funding via STFC capital grants ST/P002293/1, ST/R002371/1 and ST/S002502/1, Durham University and STFC operations grant ST/R000832/1. This work also used the DiRAC Data Intensive service at Leicester, operated by the University of Leicester IT Services, which forms part of the STFC DiRAC HPC Facility. The equipment was funded by BEIS capital funding via STFC capital grants ST/K000373/1 and ST/R002363/1 and STFC DiRAC Operations grant ST/R001014/1. DiRAC is part of the National e-Infrastructure.

REFERENCES

Aihara H., Allende Prieto C., An D., et al., 2011, *ApJS*, 193, 29
 Asplund M., Grevesse N., Sauval A. J., Scott P., 2009, *ARA&A*, 47, 481
 Baldwin J. A., Phillips M. M., Terlevich R., 1981, *PASP*, 93, 5
 Bate M. R., 2023, *MNRAS*, 519, 688
 Berg D. A., Chisholm J., Erb D. K., Skillman E. D., Pogge R. W., Olivier G. M., 2021, *ApJ*, 922, 170
 Brammer G., Valentini F., 2025, The dawn jwst archive: Compilation of public nirspec spectra (version 4.4). Zenodo
 Brucy N., Hennebelle P., Colman T., Klessen R. S., Le Yhuelic C., 2024, *A&A*, 690, A44
 Cameron A. J., Katz H., Rey M. P., 2023, *MNRAS*, 522, L89
 Campbell A., Terlevich R., Melnick J., 1986, *Monthly Notices of the Royal Astronomical Society*, 223, 811
 Chan T. K., Richings A. J., Theuns T., Liu Y., Schaller M., Ivkovic M., 2025, arXiv e-prints, arXiv:2508.13277
 Chatzikos M. et al., 2023, The 2023 release of cloudy
 Chon S., Omukai K., Schneider R., 2021, *MNRAS*, 508, 4175
 Choustikov N. et al., 2025, Megatron: Disentangling physical processes and observational bias in the multi-phase ism of high-redshift galaxies
 D'Agostino J. J., Kewley L. J., Groves B., Byler N., Sutherland R. S., Nicholls D., Leitherer C., Stanway E. R., 2019, *ApJ*, 878, 2
 Dere K. P., Del Zanna G., Young P. R., Landi E., 2023, *ApJS*, 268, 52
 Dere K. P., Landi E., Mason H. E., Monsignori Fossi B. C., Young P. R., 1997, *A&AS*, 125, 149
 Dopita M. A., Sutherland R. S., 1996, *ApJS*, 102, 161
 Draine B. T., 2011a, *ApJ*, 732, 100
 Draine B. T., 2011b, Physics of the Interstellar and Intergalactic Medium
 Elmegreen B. G., Scalo J., 2004, *ARA&A*, 42, 211
 Esteban C., Peimbert M., Garcia-Rojas J., Ruiz M. T., Peimbert A., Rodriguez M., 2004, *Monthly Notices of the Royal Astronomical Society*, 355, 229–247
 Esteban C., Peimbert M., Torres-Peimbert S., Rodriguez M., 2002, *The Astrophysical Journal*, 581, 241–257
 Eswaran V., Pope S. B., 1988, *Computers and Fluids*, 16, 257
 Federrath C., Roman-Duval J., Klessen R. S., Schmidt W., Mac Low M. M., 2010, *A&A*, 512, A81
 Ferland G. J. et al., 2017, *Rev. Mexicana Astron. Astrofis.*, 53, 385
 Ferland G. J., Korista K. T., Verner D. A., Ferguson J. W., Kingdon J. B., Verner E. M., 1998, *PASP*, 110, 761
 Garcia-Rojas J., Esteban C., 2007, *The Astrophysical Journal*, 670, 457–470
 Garnett D. R., 1992, *AJ*, 103, 1330
 Gnat O., Sternberg A., 2007, *ApJS*, 168, 213
 Gray W. J., Scannapieco E., 2017, *ApJ*, 849, 132
 Gray W. J., Scannapieco E., Kasen D., 2015, *ApJ*, 801, 107
 Grudić M. Y., Guszejnov D., Hopkins P. F., Offner S. S. R., Faucher-Giguère C.-A., 2021, *MNRAS*, 506, 2199
 Harikane Y. et al., 2025, arXiv e-prints, arXiv:2505.09186
 Jin Y., Kewley L. J., Sutherland R., 2022a, *ApJ*, 927, 37
 Jin Y., Kewley L. J., Sutherland R. S., 2022b, *ApJ*, 934, L8
 Katz H., 2022, *MNRAS*, 512, 348
 Katz H. et al., 2022, arXiv e-prints, arXiv:2211.04626
 Katz H., Rey M. P., Cadiou C., Kimm T., Agertz O., 2024, arXiv e-prints, arXiv:2411.07282
 Kauffmann G. et al., 2003, *Monthly Notices of the Royal Astronomical Society*, 346, 1055–1077
 Kewley L. J., Dopita M. A., 2002, *ApJS*, 142, 35
 Kewley L. J., Dopita M. A., Sutherland R. S., Heisler C. A., Trevena J., 2001, *ApJ*, 556, 121
 Kewley L. J., Nicholls D. C., Sutherland R., Rigby J. R., Acharya A., Dopita M. A., Bayliss M. B., 2019, *ApJ*, 880, 16
 Kewley L. J., Nicholls D. C., Sutherland R. S., 2019, *ARA&A*, 57, 511
 Kimm T., Bieri R., Geen S., Rosdahl J., Blaizot J., Michel-Dansac L., Garel T., 2022, *ApJS*, 259, 21
 Kimm T., Blaizot J., Garel T., Michel-Dansac L., Katz H., Rosdahl J., Verhamme A., Haehnelt M., 2019, *MNRAS*, 486, 2215
 Kimm T., Katz H., Haehnelt M., Rosdahl J., Devriendt J., Slyz A., 2017, *MNRAS*, 466, 4826
 Klessen R. S., Glover S. C. O., 2016, *Saas-Fee Advanced Course*, 43, 85
 Kobulnicky H. A., Kennicutt, Jr. R. C., Pizagno J. L., 1999, *ApJ*, 514, 544
 Kumar S., Chen H.-W., 2025, *The Open Journal of Astrophysics*, 8, 98
 Larson R. B., 1981, *MNRAS*, 194, 809
 Lebouteiller V., Ramambason L., 2022, *A&A*, 667, A34
 Luridiana V., Morisset C., Shaw R. A., 2015, *A&A*, 573, A42
 Marconi A. et al., 2024, *A&A*, 689, A78
 Martinez Z. et al., 2025, arXiv e-prints, arXiv:2510.21960
 McClymont W., Smith A., Tacchella S., 2025, arXiv e-prints, arXiv:2510.13952
 Méndez-Delgado J. E. et al., 2023, *MNRAS*, 523, 2952
 Menon S. H., Burkhardt B., Somerville R. S., Thompson T. A., Sternberg A., 2025, *ApJ*, 987, 12
 Menzel D. H., Aller L. H., Hebb M. H., 1941, *ApJ*, 93, 230
 Nicholls D. C., Dopita M. A., Sutherland R. S., 2012, *The Astrophysical Journal*, 752, 148
 Peimbert Á., Peimbert M., 2013, *The Astrophysical Journal*, 778, 89
 Peimbert M., 1967, *ApJ*, 150, 825
 Pérez-Montero E., Diaz A. I., 2003, *MNRAS*, 346, 105
 Richings A. J., Faucher-Giguère C.-A., Gurvich A. B., Schaye J., Hayward C. C., 2022, *MNRAS*, 517, 1557
 Rosdahl J., Blaizot J., Aubert D., Stranex T., Teyssier R., 2013, *MNRAS*, 436, 2188
 Rosdahl J., Teyssier R., 2015, *MNRAS*, 449, 4380
 Rubin R. H., 1968, *ApJ*, 153, 761
 Sanders R. L. et al., 2025, arXiv e-prints, arXiv:2508.10099
 Smith A., Safranek-Shrader C., Bromm V., Milosavljevic M., Kimock B., Garaldi E., Yeh J. Y.-C., 2023, COLT: Monte Carlo radiative transfer and simulation analysis toolkit. Astrophysics Source Code Library, record ascl:2306.034
 Spitzer L., 1978, Physical processes in the interstellar medium
 Stasinska G., 1978, *A&A*, 66, 257
 Stasinska G., 1982, *A&AS*, 48, 299
 Stasinska G., 2005, *Astronomy and Astrophysics*, 434, 507–520
 Sutherland R., Dopita M., Binette L., Groves B., 2018, MAPPINGS V: Astrophysical plasma modeling code. Astrophysics Source Code Library, record ascl:1807.005
 Teyssier R., 2002, *A&A*, 385, 337
 Vaught R. J. R. et al., 2024, Investigating the drivers of electron temperature variations in hii regions with keck-kcwi and vlt-muse
 Veilleux S., Osterbrock D. E., 1987, *ApJS*, 63, 295
 Wang W., Liu X.-W., Zhang Y., Barlow M. J., 2004, *Astronomy and Astrophysics*, 427, 873–886
 Yuan H.-B., Liu X.-W., Péquignot D., Rubin R. H., Ercolano B., Zhang Y., 2010, *Monthly Notices of the Royal Astronomical Society*, 411, 1035–1052
 Ziegler U., 2018, *A&A*, 620, A81

provides fast and easy peer review for new papers in the **astro-ph** section of the arXiv, making the reviewing pro-

cess simpler for authors and referees alike. Learn more at <http://astro.theoj.org>.